Subducting Slab Ultra-Slow Velocity Layer Coincident with Silent Earthquakes in Southern Mexico

Teh-Ru Alex Song, *et al.*

Science **324**, 502 (2009);
DOI: 10.1126/science.1167595

Science (print ISSN 0036-8075; online ISSN 1095-9203) is published weekly, except the last week in December, by the American Association for the Advancement of Science, 1200 New York Avenue NW, Washington, DC 20005.

References and Notes

1. B. Gutenberg, *Physics of the Earth's Interior* (Elsevier, New York, 1959).
2. H. Kanamori, F. Press, *Nature* **226**, 330 (1970).
3. S. Karato, H. Jung, *Earth Planet. Sci. Lett.* **157**, 193 (1998).
4. G. Hirth, D. Kohlstedt, *Earth Planet. Sci. Lett.* **144**, 93 (1996).
5. P. Kumar, X. Yuan, R. Kind, J. Ni, *J. Geophys. Res.* **111**, 10.1029/2005JB003930 (2006).
6. C. A. Rychert, K. M. Fischer, S. Rondenay, *Nature* **436**, 542 (2005).
7. Y. Fukao *et al.*, in *Workshop Report of OHP/ION Joint Symposium, Long-Term Observations in the Oceans* (Earthquake Research Institute, Univ. of Tokyo, Tokyo, Japan, 2001), pp. 13–29.
8. M. Shinohara *et al.*, *Ann. Geophys.* **49**, 625 (2006).
9. M. Shinohara *et al.*, *Phys. Earth Planet. Inter.* **170**, 95 (2008).
10. Materials and methods are available as supporting material on *Science* Online.
11. L. P. Vinnik, *Phys. Earth Planet. Inter.* **15**, 39 (1977).
12. C. A. Langston, *J. Geophys. Res.* **84**, 4749 (1979).
13. V. Farra, L. Vinnik, *Geophys. J. Int.* **141**, 699 (2000).
14. H. Kawakatsu, S. Watada, *Science* **316**, 1468 (2007).
15. T. Tonegawa, K. Hirahara, T. Shibutani, N. Fujii, *Earth Planet. Sci. Lett.* **247**, 101 (2006).
16. K. Mierdel, H. Keppler, J. R. Smyth, F. Langenhorst, *Science* **315**, 364 (2007).
17. S. Honda, D. A. Yuen, *Geophys. Res. Lett.* **28**, 351 (2001).
18. The thermal model is constructed incorporating the pressure and temperature effect on the thermal diffusivity; among the range of models that give similar fit to surface observables (*29*), one with the plate thickness of 104 km and the temperature at the base of plate 1358°C (corresponding to a potential temperature of 1315°C) is used.
19. Y. Takei, *J. Geophys. Res.* **107**, 10.1029/2001JB000522 (2002).
20. J. Langmuir, E. M. Klein, T. Plank, in *Mantle Flow and Melt Generation at Mid-Ocean Ridges* (American Geophysical Union, Washington, DC, 1992), pp. 183–200.
21. B. K. Holtzman *et al.*, *Science* **301**, 1227 (2003).
22. R. F. Katz, M. Spiegelman, B. Holtzman, *Nature* **442**, 676 (2006).
23. G. E. Backus, *J. Geophys. Res.* **67**, 4427 (1962).
24. M. Takaku, Y. Fukao, *Phys. Earth Planet. Inter.* **166**, 44 (2008).
25. Y. Takei, B. K. Holtzman, *J. Geophys. Res.*, in press.
26. G. Ekström, A. M. Dziewonski, *Nature* **394**, 168 (1998).
27. K. Baba, A. D. Chave, R. L. Evans, G. Hirth, R. L. Mackie, *J. Geophys. Res.* **111**, B02101 (2006).
28. Y. Gung, M. Panning, B. Romanowicz, *Nature* **422**, 707 (2003).
29. C. A. Stein, S. Stein, *Nature* **359**, 123 (1992).
30. In the wet asthenosphere model, the velocity contrast is estimated from the relation between η_0/η and V_S/V_S^0 (*3*) (blue dotted line) and $\eta_0/\eta \cong 100$ (*4*). In the partially molten asthenosphere model, viscosity of grain-boundary diffusion creep and elasticity are calculated for each layer by granular models (*19*, *25*), and effective properties of layered medium are calculated by the Backus average (*23*). In the layered model, η_0/η shows the contrast for horizontal shear flow, and V_S/V_S^0 shows the contrast of equivalent isotropic media, which give the same amplitude of *S*-to-*P* phase for the incident angle of 25° (typical for this study) (*10*).
31. B. Holtzman's drawing [figure 12 of (*25*)] was the inspiration for the proposed model of the melt-segregated shear zone in the asthenosphere. We thank S. Honda for the computer code to calculate the thermal structure and T. Inoue and K. Mibe for discussions. P.K. is supported by the JSPS fellowship provided by the Japan Society for the Promotion of Science. OHP was funded by the Ministry of Education, Culture, Sports, Science, and Technology of Japan.

Supporting Online Material

www.sciencemag.org/cgi/content/full/324/5926/499/DC1
Materials and Methods
Figs. S1 to S11
References

9 December 2008; accepted 26 February 2009
10.1126/science.1169499

Subducting Slab Ultra-Slow Velocity Layer Coincident with Silent Earthquakes in Southern Mexico

Teh-Ru Alex Song,[1]* Donald V. Helmberger,[2] Michael R. Brudzinski,[3] Robert W. Clayton,[2] Paul Davis,[4] Xyoli Pérez-Campos,[5] Shri K. Singh[5]

Great earthquakes have repeatedly occurred on the plate interface in a few shallow-dipping subduction zones where the subducting and overriding plates are strongly locked. Silent earthquakes (or slow slip events) were recently discovered at the down-dip extension of the locked zone and interact with the earthquake cycle. Here, we show that locally observed converted *SP* arrivals and teleseismic underside reflections that sample the top of the subducting plate in southern Mexico reveal that the ultra-slow velocity layer (USL) varies spatially (3 to 5 kilometers, with an *S*-wave velocity of ~2.0 to 2.7 kilometers per second). Most slow slip patches coincide with the presence of the USL, and they are bounded by the absence of the USL. The extent of the USL delineates the zone of transitional frictional behavior.

Silent earthquakes, or episodic slow slip events (SSEs), and nonvolcanic tremor have been observed in a few shallow subduction zones such as Cascadia (*1*–*3*), southwest Japan (*4*–*6*), and southern Mexico (*7*–*15*). In general, most slow slip and tremor activities take place at the transition zone down-dip of the strong coupling section, where great thrust earthquakes occur. In southern Mexico, the Cocos plate is subducting underneath the North America plate, where the slab is almost flat near Guerrero (*16*) and is at a low angle near Oaxaca (Fig. 1) (*17*). SSEs with moment magnitudes M_w of ~7 to 7.5 occur every 1 to 2 years (Fig. 1) (*7*–*11*, *18*, *19*). However, the locations of SSEs vary along-strike, extending about 150 km inland from the Guerrero coast (*7*–*10*, *18*) but are limited to within 100 km near Oaxaca (Fig. 1) (*11*, *15*). In addition, nonvolcanic tremor (NVT) concentrates near the down-dip end of the slow-slip zone (*12*–*14*). This along-strike variation in the location of SSEs and NVT can be compared with the seismic structure of the subducting plate to investigate if the location variation is structurally controlled. We examined locally converted *SP* waves from intraslab earthquakes to map out the seismic structure at the top of the subducting slab beneath southern Mexico (*20*).

SP waves start as shear waves radiated from intraslab earthquakes and convert to *P* waves at the sharp velocity contrast on the plate interface. They are particularly useful for examining a slab structure directly above the source (Fig. 2A) (*21*). The *SP* wave typically arrives 2 to 3 s after the direct *P* wave, depending on the depth of an earthquake (*20*). In this study, we model the first 7 s of the broadband *P* waveforms (0.01 to 0.6 Hz) to explain the interference between the direct *P* wave and the *SP* wave, which ultimately provides a high-resolution map of the upper slab structure (*20*). Our data include two moderate intraslab events recorded by the temporary Meso-American Subduction Experiment (MASE) (*17*) and 40 intraslab events from 1990 to 2008 [body wave magnitude (M_b) = 4.5 ~ 6.0] recorded by the permanent GEOSCOPE station UNM (Fig. 1 and fig. S1).

As an example, we display *P* waveforms recorded at station PTRP and station SAME farther to the north to illustrate how the waveform changes with position (Fig. 2B). The timing of the first negative pulse (pulse A) after the direct *P* wave is consistent with an *SP* arrival, but its amplitude is anomalously large at station PTRP. We can model the *SP* wave that was converted from the bottom of an ultra-slow velocity layer [USL; 3 km and a *S*-wave velocity (V_s) of ~2.7 km/s] directly above the source region. The pulse with a positive polarity (pulse B) immediately following the pulse A is an *SP* arrival converted from the top of the USL. A series of

[1]Department of Terrestrial Magnetism, Carnegie Institution of Washington, 5241 Broad Branch Road N.W., Washington, DC 20015, USA. [2]Seismological Laboratory, Division of Geological and Planetary Science, California Institute of Technology, 1200 East California Boulevard, Pasadena, CA 91125, USA. [3]Department of Geology, Miami University, 114 Shideler Hall, Oxford, OH 45056, USA. [4]Department of Earth and Space Sciences, Center of Embedded Network Systems (CENS), University of California, Los Angeles (UCLA), 595 Charles Young Drive East, Los Angeles, CA 90095–1567, USA. [5]Instituto de Geofísica, Universidad Nacional Autónoma de México, Circuito de la Investigación Científica s/n, Ciudad Universitaria, D.F. 04510 Distrito Federal, México.

*To whom correspondence should be addressed. E-mail: asong@ciw.edu

synthetic tests demonstrate that the amplitude of pulse A and pulse B and their relative timing are primarily determined by the *S* wave velocity and the thickness of the USL (fig. S2). However, the interpretation of the pulse C, which arrived about 1.5 s after the direct *P* wave, is less obvious (Fig. 2B). Synthetic tests demonstrate that introducing a low velocity layer [LVL; 22 km and a *P*-wave velocity (V_p) of ~7.5 km/s] directly below the USL can reproduce a turning *P* wave from the bottom of the LVL with correct timing and amplitude (Fig. 2B). The amplitude of the pulse C increases with the velocity contrast between the LVL and the underlying fast slab, whereas its timing is controlled by the separation between the source and the lower boundary of the LVL (fig. S2). In this report, we focus on the USL and its lateral variation.

About 30 events were recorded by station UNM that display waveforms similar to those recorded by station PTRP above (Fig. 1), demonstrating a similar slab structure above the various sources. We can reproduce the characteristics of these waveforms and their variability by moving the source location to match the differential behavior between the *P* wave and converted *SP* arrival (fig. S3). Our best-fitting model consists of a thin USL of ~3 to 5 km and shear velocity of about 2.0 to 2.7 km/s. The contrast in *S* wave velocity across the bottom of the USL is about 26 to 40%. In general, the data are well-explained (Fig. 1 and figs. S4 to S5).

Broadband waveforms from the other 13 events are similar [Fig. 1, black waveforms (far right) and white circles] but have much smaller *SP* arrivals. These data do not require the prominent USL described above (fig. S6). However, the amplitude of *SP* arrivals, particularly for pulse A, from events such as 13 and 21 are smaller than that of the 28 events but slightly larger than that of other events near Oaxaca. These data suggest that seismic velocity near the top of the slab varies both parallel and normal to the trench (Fig. 1). Cases without the USL are all farther inland than cases with the USL. Furthermore, the MASE data from an event located beneath west Guerrero display a systematic decrease in *SP* amplitude toward the north (Fig. 1, top left inset) over distances of <10 km. On the basis of these observations, it is clear that the USL is confined to within 150 km of the coast in Guerrero. Data from events such as 1, 2, 4, 5, and 7 near Oaxaca do not reveal the USL, suggesting that it extends probably no more than 100 km from the coast near Oaxaca.

If the spatial variation in the presence of the USL is reasonably constrained by the local *SP* arrival, our model should be able to explain other independent data from these same events. In particular, by stacking teleseismic *P* waves recorded by the Yellowknife array, we can identify the depth phases such as *pP* and *sP* (Fig. 3A and fig. S7). The prominence of the depth phase *sP* is favorable to further search for the underside reflection ($s_{USL}P$) from the USL (Fig. 3B). Indeed, an additional strong phase arrived about 3.5 to 4 s after the first *P* wave of event 27. Its timing and amplitude are consistent with the $s_{USL}P$ from the USL. Variations

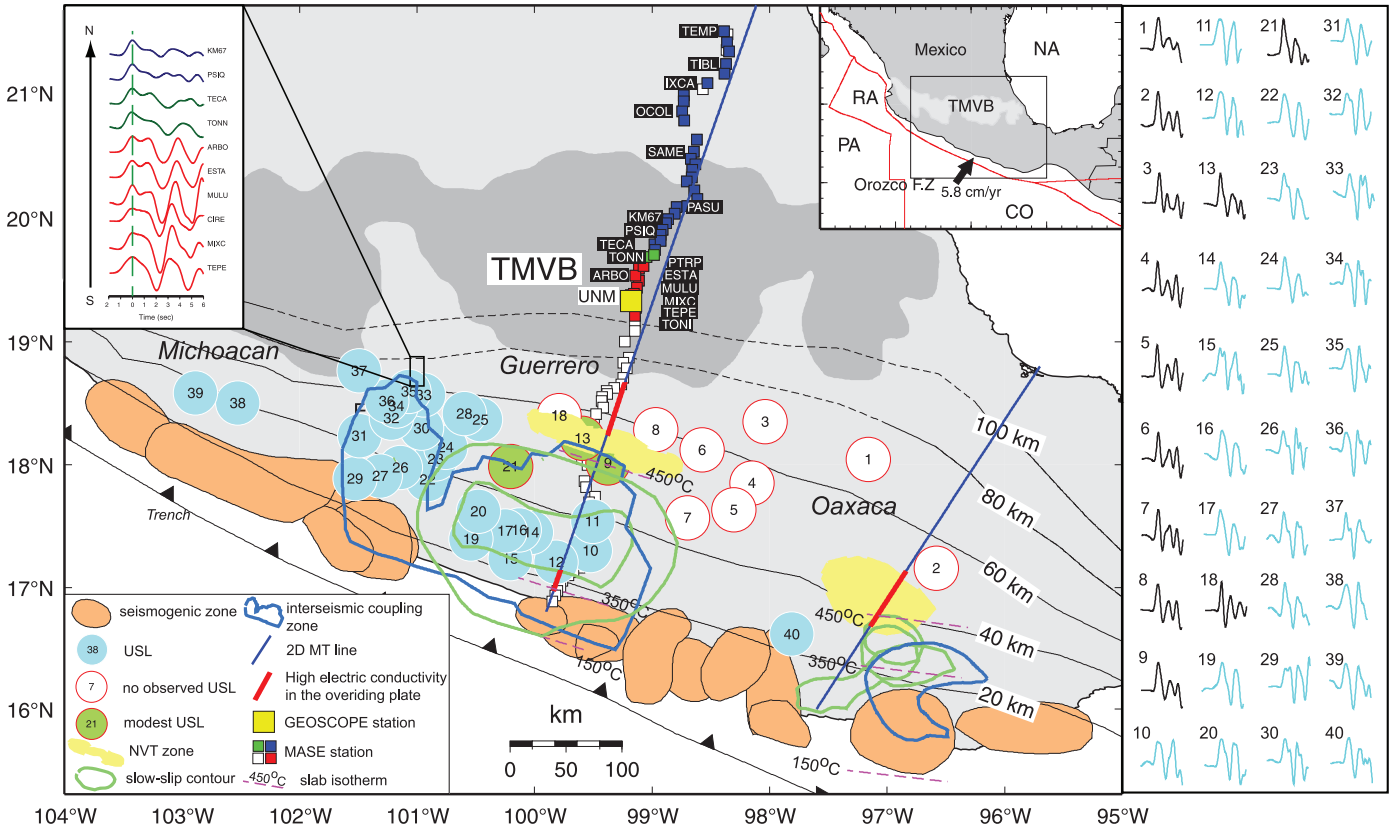

Fig. 1. Mapping of the USL beneath southern Mexico. The top right inset shows the regional tectonic setting where the Cocos plate (CO) is subducting beneath the North America plate (NA). RA, Rivera plate; PA, Pacific plate. The red line delineates the plate boundary. The enlarged map shows geophysical observables and seismic sampling. Shown is the nearly flat portion of the slab beneath the Guerrero province (*16*). *P* wave displacement data (0.01 to 0.6 Hz) recorded on the vertical component of the GEOSCOPE station UNM are displayed on the far right. Data associated with blue circles (blue traces) are characterized by a large converted *SP* wave arriving about 2 to 3 s after the first *P* wave, whereas data associated with white circles (black traces) are without such a strong negative pulse. Data associated with light green circles are with a converted *SP* arrival but are less strong. The spatial extent of the USL (blue circles) coincides with the location of large slow slip patches (green contours) and interseismic coupling (blue contours) (*18*). NVT occurs along the transition from blue circles to white circles where electric resistivity is relatively high (~ 200 ohm m) in the overriding plate (indicated by the red segments in the two-dimensional magnetotelluric lines (dark blue lines across Guerrero and Oaxaca) (*26*). Abrupt decrease in the amplitude of the *SP* arrival from stations ARBO to PSIQ (top left panel) also indicates the north limit of the USL (solid rectangle).

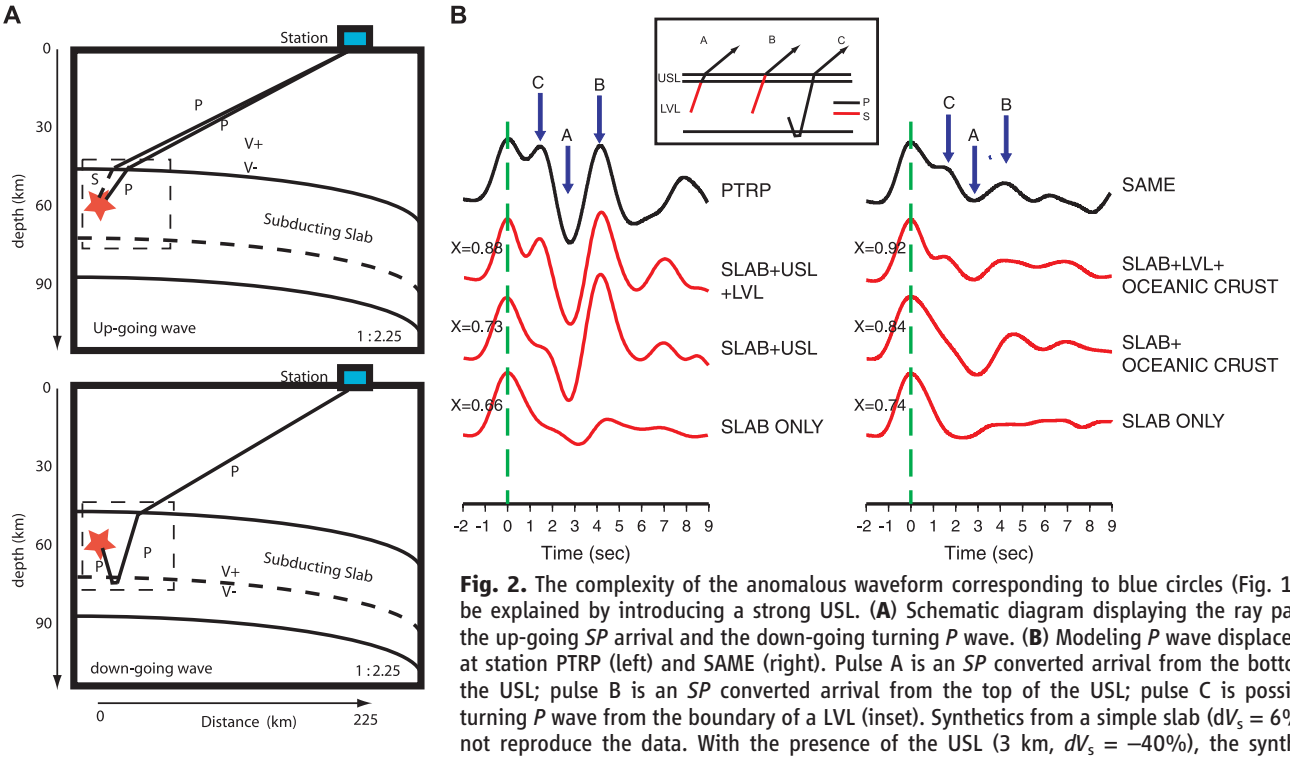

Fig. 2. The complexity of the anomalous waveform corresponding to blue circles (Fig. 1) can be explained by introducing a strong USL. (**A**) Schematic diagram displaying the ray path of the up-going *SP* arrival and the down-going turning *P* wave. (**B**) Modeling *P* wave displacement at station PTRP (left) and SAME (right). Pulse A is an *SP* converted arrival from the bottom of the USL; pulse B is an *SP* converted arrival from the top of the USL; pulse C is possibly a turning *P* wave from the boundary of a LVL (inset). Synthetics from a simple slab (dV_s = 6%) do not reproduce the data. With the presence of the USL (3 km, dV_s = −40%), the synthetics explain the pulse A and pulse B at station PTRP. But data recorded at station SAME to the north do not require the USL, and we can model it as a hydrated oceanic crust with dV_s = −20%. We assume $d\ln V_s/d\ln V_p$ = 2 in the USL and LVL. *X* is the coefficient of cross-correlation between data and synthetics.

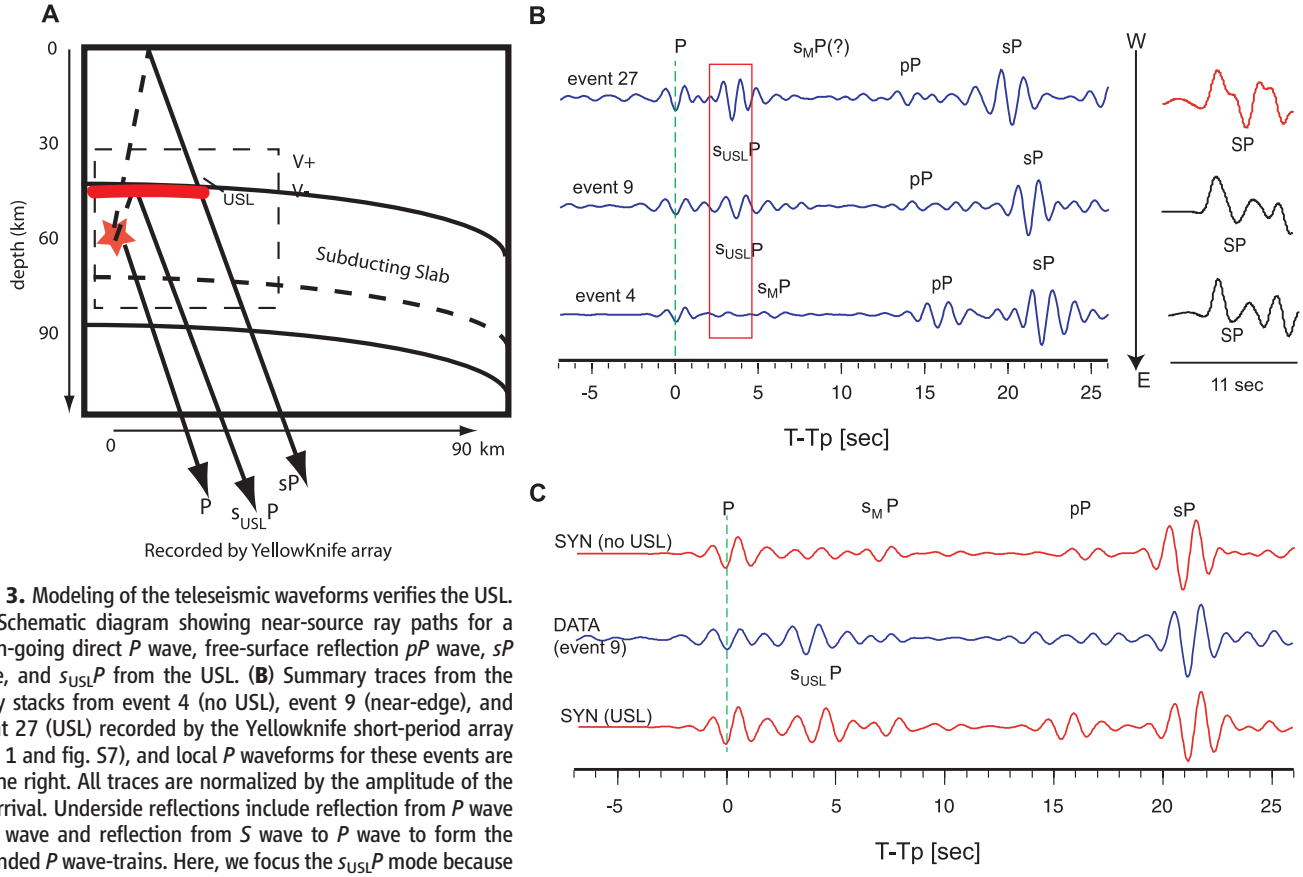

Fig. 3. Modeling of the teleseismic waveforms verifies the USL. (**A**) Schematic diagram showing near-source ray paths for a down-going direct *P* wave, free-surface reflection *pP* wave, *sP* wave, and $s_{USL}P$ from the USL. (**B**) Summary traces from the array stacks from event 4 (no USL), event 9 (near-edge), and event 27 (USL) recorded by the Yellowknife short-period array (Fig. 1 and fig. S7), and local *P* waveforms for these events are on the right. All traces are normalized by the amplitude of the *sP* arrival. Underside reflections include reflection from *P* wave to *P* wave and reflection from *S* wave to *P* wave to form the extended *P* wave-trains. Here, we focus the $s_{USL}P$ mode because of its large amplitude. s_MP is the underside reflection from the continental Moho arriving 7 to 9 s after the *P* wave, but it is not prominent. Data from event 27 beneath west Guerrero show the largest $s_{USL}P$ relative to *sP*, whereas the amplitude of the $s_{USL}P$ decreases toward the east. This observation is consistent with the amplitude of the local *SP* wave. (**C**) Predictions match the amplitude of the $s_{USL}P$ from event 9 when the USL has half the velocity reduction needed to model event 27. Synthetics computed from the model without the USL explain the data from event 4.

in the amplitude of the teleseismic $s_{USL}P$ are consistent with the amplitude of the local converted *SP* wave from the same intraslab events (Fig. 3B). Our model, which was derived from modeling local converted *SP* waves, can reasonably predict these teleseismic $s_{USL}P$, their along-strike variations, and teleseismic $s_{USL}S$ (Fig. 3C and fig. S8). Moreover, teleseismic receiver function analysis directly beneath the MASE line (*16*) also reveals strong evidence of an uneven but continuous LVL extending to the southern end of the Trans-Mexican Volcanic Belt (TMVB) and is generally consistent with the USL sampled by the regional *SP* waves near the array. A relatively weak receiver function pulse from 130 to 170 km from the coast (*16*) is also consistent with weaker *SP* waves (Fig. 1, green circles). Complexities do exist near event 13, possibly because of lateral variations in the down-dip extent of the USL near the MASE array.

The *S*-wave velocity of the USL (2.0 to 2.7 km/s) is 30 to 54% slower than that of the hydrated ocean crust at the depth of 25 to 50 km, which is typically in the 3.8 to 4.4 km/s range (*22*). The *S* wave velocity across the bottom of the USL (~26 to 40%) also exceeds the velocity contrast predicted for hydrated oceanic crust and oceanic mantle (*22*). Although partial melting of oceanic crust can drastically decrease *S* wave velocity, thermal modeling of the slab (*23*, *24*) suggested that temperatures probably are too low. Alternatively, the USL may represent the oceanic crust (or part of the oceanic crust) that is fluid-saturated, forming a high pore-fluid pressure layer (HPFP) with a porosity (ϕ) of ~2 to 3.5% and aspect ratio α of ~0.01 (*25*). These estimates are consistent with local electric resistivity of ~200 ohm m in the overriding plate that was obtained from magnetotelluric studies in southern Mexico (*26*).

We find that the spatial extent of the HPFP layer coincides well with the region close to the coast near Guerrero, where slow slip is well documented and the sampling of the slab is denser. Both seem to be located in a region bounded by the 350 and 450°C isotherms predicted for the plate interface (*23*, *24*), where there is interseismic coupling (*7*, *15*, *18*). The HPFP layer could potentially extend farther up-dip than observed before the plate interface reaches temperatures of >350°C. Most NVT locations are concentrated in the upper plate north of where the prominent HPFP layer occurs at the plate interface and where electric conductivity in the upper plate is relatively high (Fig. 1). Although the sampling of the slab near Oaxaca is sparse, we find similar relations there, supporting a direct spatial correlation of the HPFP layer and SSEs with NVT and high conductivity again to the north. Examining all of the events between 99°W and 102°W with evidence for the USL (Fig. 1), events 35, 37, 22, and 34 clearly show the HPFP layer is present during the SSEs (Fig. 1 and fig. S9). Although these events primarily occur west of the slow slip contour in Fig. 1, the western extent of slow slip is not well known. Furthermore, the HPFP layer also exists during the inter-SSE period (fig. S9), indicating that the HPFP layer is persistent over at least the 20 years of our data.

Our interpretation (Fig. 4) is that a transition zone at shallow depths on the plate interface lies below the region where interseismic coupling is strong. It is partially coupled during the interseismic period, resulting in episodic slow slip at the down-dip end of the seismogenic zone at regions with temperatures ranging from 350 to 450°C (*24*). NVT sources concentrate near the down-dip end of the transition zone around 450°C, where blueschist-eclogite dehydration reactions are predicted to occur at depths near 40 to 50 km (*22*). Fluid released from this reaction could percolate into the overriding plate, produce observed high electric conductivity, and probably trigger the NVT. Fluids appear to be trapped up-dip in a HPFP layer and it is probably controlled by material-dependent permeability and fluid generation processes near the interface (*20*). The spatial extent of the HPFP layer provides a natural explanation for the occurrence of SSEs and NVT because it would be expected to greatly reduce the effective normal stress on the plate interface, promoting episodic slow slip (*27*) and the dynamic triggering of tremors (*28*).

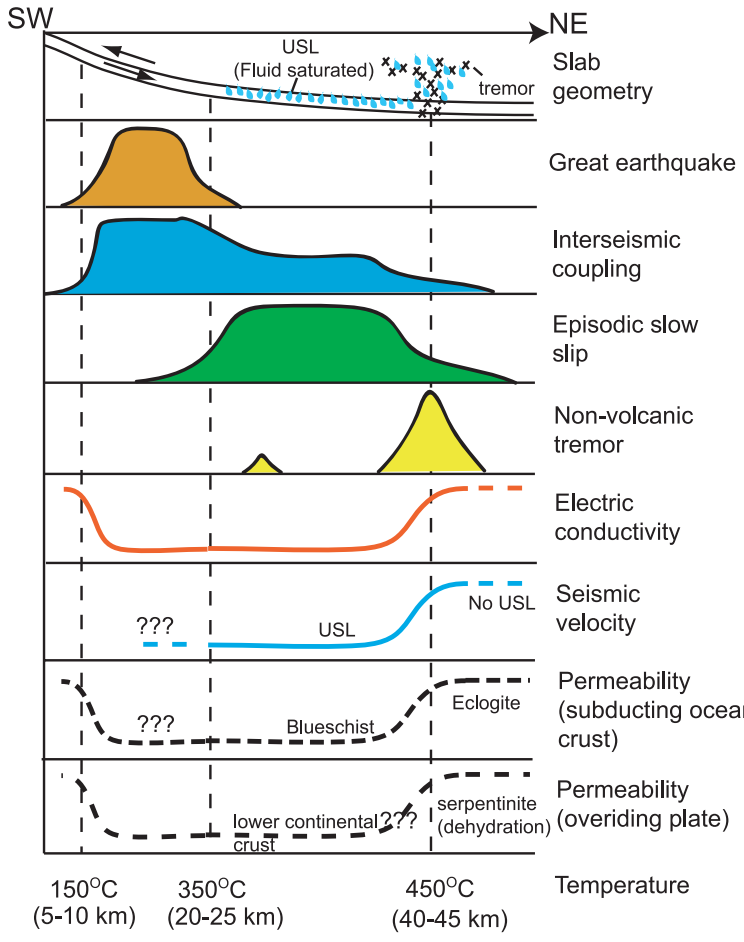

Fig. 4. A schematic cross section of the slab geometry along with observations that were used to make the interpretation. Dotted lines indicate the slab isotherm. The various panels include variations in the location of great earthquakes, interseismic coupling, SSEs, NVT, electric conductivity, seismic velocity, and inferred permeability (*20*). Blue drops indicate the presence of fluids, and x's indicate NVT cavities.

References and Notes

1. H. Dragert, K. Wang, T. S. James, *Science* **292**, 1525 (2001).
2. G. Rogers, H. Dragert, *Science* **300**, 1942 (2003).
3. H. Kao *et al.*, *Nature* **436**, 841 (2005).
4. K. Obara, *Science* **296**, 1679 (2002).
5. S. Zawa *et al.*, *Geophys. Res. Lett.* **31**, 10.1029/2003GL019381 (2004).
6. D. R. Shelly, G. C. Beroza, S. Ide, S. Nakamula, *Nature* **442**, 188 (2006).
7. V. Kostoglodov *et al.*, *Geophys. Res. Lett.* **30**, 10.1029/2003GL017219 (2003).
8. K. M. Larson *et al.*, *J. Geophys. Res.* **109**, 10.1029/2003JB002843 (2004).
9. A. R. Lowry, *Nature* **442**, 802 (2006).
10. K. M. Larson, V. Kostoglodov, S. Miyazaki, J. A. Santiago, J. A. *Geophys. Res. Lett.* **34**, 10.1029/2007GL029912 (2007).
11. M. Brudzinski, E. Cabral-Cano, F. Correa-Mora, C. DeMets, B. Márquez-Azúa, *Geophys. J. Int.* **171**, 523 (2007).
12. M. Brudzinski, E. Cabral-Cano, A. Arciniega-Ceballos, C. DeMets, O. Diaz-Molina, *Eos Trans. AGU* **88**(23), abstract G31A-02 (2007).
13. H. R. Hinojosa-Prieto *et al.*, *EOS Trans. AGU* **88**, abstract T21A-0350 (2007).

14. J. S. Payero *et al.*, *Geophys. Res. Lett.* **35**, 10.1029/2007GL032877 (2008).
15. F. Correa-Mora, C. DeMets, E. Cabral-Cano, B. Marquez-Azua, O. Diaz-Molina, *Geophys. J. Int.* **175**, 269 (2008).
16. X. Perez-Campos *et al.*, *Geophys. Res. Lett.* **35**, 10.1029/2008GL035127 (2008).
17. M. Pardo, G. Suárez, *J. Geophys. Res.* **100**, 12357 (1995).
18. S. Yoshioka *et al.*, *Phys. Earth Planet Inter.* **146**, 513 (2004).
19. A. Iglesias *et al.*, *Geofis. Int.* **43**, 309 (2004).
20. Materials and methods are available as supporting material on *Science* Online.
21. T. Matsuzawa, T. Kono, A. Hasegawa, A. Takagi, *Tectonophysics* **181**, 123 (1990).
22. B. R. Hacker, G. A. Abers, S. M. Peacock, *J. Geophys. Res.* **108**, 10.1029/2001JB001127 (2003).
23. V. Manea, M. Manea, V. Kostoglodov, C. A. Currie, G. Sewell, *Geophys. J. Int.* **158**, 775 (2004).
24. C. A. Currie, R. D. Hyndman, K. Wang, V. Kostoglodov, *J. Geophys. Res.* **107**, 10.1029/2001JB000886 (2002).
25. Y. Takei, *J. Geophys. Res.* **107**, 10.1029/2001JB000522 (2002).
26. H. Jödicke *et al.*, *J. Geophys. Res.* **111**, 10.1029/2005JB003739 (2006).
27. Y. Liu, J. R. Rice, *J. Geophys. Res.* **112**, 10.1029/2007JB004930 (2007).
28. J. L. Rubinstein *et al.*, *Nature* **448**, 579 (2007).
29. We thank S. Sacks, P. Silver, S. Shirey, M. Bostock, J.-P. Avouav, and V. Manea for helpful discussions; R. Engdahl provided the global relocated seismic catalog used in fig. S10. We thank CENS at UCLA for support and the entire MASE team for making the MASE data available. We thank H. Hinojosa-Prieto, E. Cabral-Cano, A. Arciniega, O. Diaz-Molina, and C. DeMets for sharing their work on episodic tremor and slip in Oaxaca. Incorporated Research Institutions for Seismology Data Management Center and Canadian National Data Centre provided the GEOSCOPE data and Yellowknife short-period data used in this analysis, respectively. Station UNM is operated and maintained by Servicio Sismológical Nacional. This work is partially supported by NSF grant EAR-0636012. This is Tectonic Observatory contribution 10015. T.-R.A.S. is supported by a Carnegie fellowship at the Department of Terrestrial Magnetism.

Supporting Online Material

www.sciencemag.org/cgi/content/full/324/5926/502/DC1
Materials and Methods
SOM Text
Figs. S1 to S11
Table S1
References

23 October 2008; accepted 20 February 2009
10.1126/science.1167595

$^{14}CH_4$ Measurements in Greenland Ice: Investigating Last Glacial Termination CH_4 Sources

Vasilii V. Petrenko,[1]*† Andrew M. Smith,[2] Edward J. Brook,[3] Dave Lowe,[4] Katja Riedel,[4] Gordon Brailsford,[4] Quan Hua,[2] Hinrich Schaefer,[4] Niels Reeh,[5] Ray F. Weiss,[1] David Etheridge,[6] Jeffrey P. Severinghaus[1]

The cause of a large increase of atmospheric methane concentration during the Younger Dryas–Preboreal abrupt climatic transition (~11,600 years ago) has been the subject of much debate. The carbon-14 (^{14}C) content of methane ($^{14}CH_4$) should distinguish between wetland and clathrate contributions to this increase. We present measurements of $^{14}CH_4$ in glacial ice, targeting this transition, performed by using ice samples obtained from an ablation site in west Greenland. Measured $^{14}CH_4$ values were higher than predicted under any scenario. Sample $^{14}CH_4$ appears to be elevated by direct cosmogenic ^{14}C production in ice. ^{14}C of CO was measured to better understand this process and correct the sample $^{14}CH_4$. Corrected results suggest that wetland sources were likely responsible for the majority of the Younger Dryas–Preboreal CH_4 rise.

Ice core records from Greenland and Antarctica show large and rapid variations in atmospheric methane (CH_4) concentrations ($[CH_4]$) in response to climate change (*1*). One such rapid $[CH_4]$ increase occurred at the Younger Dryas (YD)–Preboreal (PB) [~11,600 years before present (B.P.), in which 0 B.P. = 1950 A.D.] abrupt warming event during the last deglaciation (Fig. 1). The causes of these rapid $[CH_4]$ fluctuations have been the subject of intense debate. Several modeling studies suggest that glacial-interglacial changes in the atmospheric concentration of OH radicals (the main CH_4 sink) were small (*2*, *3*). It is thus likely that the observed rapid $[CH_4]$ increases were driven mostly by increases in CH_4 sources.

Several hypotheses regarding such sources have been proposed, including increased emissions from wetlands (*4*), marine clathrates (*5*, *6*), and, more recently, thermokarst lakes (*7*). The possibility of CH_4 clathrate reservoir instability in response to climatic warming is particularly troubling in the light of present anthropogenic warming. If only 10% of CH_4 from the modern clathrate reservoir (which has ~5000 Pg of C) were to be released to the atmosphere in a few years, the radiative forcing would be equivalent to a 10-fold increase in $[CO_2]$ (*8*).

In an attempt to better understand past changes in the CH_4 budget, two records of carbon-13/carbon-12 ratio ($\delta^{13}C$) (*9*, *10*) and one record of deuterium/hydrogen ratio (δD) (*11*) of CH_4 from ice cores spanning the last glacial termination have recently been produced. Unfortunately, $\delta^{13}CH_4$ of many major CH_4 sources is similar (*12*), imperfectly known (*13*), and influenced by climatic conditions (*14*), limiting the utility of $\delta^{13}CH_4$ for testing different hypotheses for the rapid $[CH_4]$ increases. δD of CH_4 is a more promising tracer for this purpose, because the δD of clathrate CH_4 is much higher than that of wetland emissions (*11*). The Greenland Ice Sheet Project 2 (GISP2) ice core record (Fig. 1) showed no significant change in δD of CH_4 through the YD-PB transition, which is evidence against major clathrate involvement (*11*).

The best tracer for distinguishing between the clathrate and wetland hypotheses is arguably $^{14}CH_4$. The ultimate source of C for wetland-produced CH_4 is essentially contemporaneous atmospheric CO_2 (*15*). If wetlands were the only source of the rapid $[CH_4]$ rise, there should be either no change or an increase in $^{14}CH_4$ after the abrupt warming event. In contrast, CH_4 clathrates are geologically old and contain little or no measurable ^{14}C (*16*). If clathrates were the only source of the $[CH_4]$ rise, $^{14}CH_4$ over the transition would decrease (Fig. 1). In addition, paleoatmospheric $^{14}CH_4$ measurements should allow for straightforward quantification of the strength of the geologic CH_4 source, which may be an important term in the global CH_4 budget (*17*).

We used a surface outcrop named Pakitsoq on the west Greenland ice margin (*18*–*20*) to obtain ~1000-kg-sized glacial ice samples containing ancient air from the YD-PB transition and yielding ~ 20 μg of CH_4 carbon per sample for ^{14}C measurements. Air was melt-extracted from sample ice in the field (*20*, *21*). We dated the sampled ice and occluded air using a combination of $\delta^{15}N$ of N_2, $\delta^{18}O$ of O_2, $\delta^{18}O$ of ice ($\delta^{18}O_{ice}$), and $[CH_4]$ measurements (*21*), which uniquely identified the age of the sampled section. Sample CH_4 was separated from bulk air by means of combustion to CO_2 on platinized quartz wool followed by cryogenic trapping (*20*, *22*). CH_4-derived CO_2 was converted to graphite and measured for ^{14}C by means of accelerator mass spectrometry (*20*, *22*).

$^{14}CH_4$ results are presented in Fig. 1 and table S1. Surprisingly, all values are higher than ^{14}C of contemporaneous CO_2; that is, above the highest expected paleoatmospheric $^{14}CH_4$. Procedural ^{14}C contamination was shown through extensive testing to be very small (<3% of sample

[1]Scripps Institution of Oceanography, University of California, San Diego, La Jolla, CA 92093, USA. [2]Australian Nuclear Science and Technology Organisation (ANSTO), Private Mail Box 1, Menai, NSW 2234, Australia. [3]Department of Geosciences, Oregon State University, Corvallis, OR 97331, USA. [4]National Institute of Water and Atmospheric Research Ltd., Post Office Box 14901, Kilbirnie, 301 Evans Bay Parade, Wellington, New Zealand. [5]DTU Space, National Space Institute, Technical University of Denmark, Ørsteds Plads, Building 348, DK-2800 Kongens Lyngby, Denmark. [6]Commonwealth Scientific and Industrial Research Organisation, Marine and Atmospheric Research, Private Mail Box 1, Aspendale, VIC 3195, Australia.

*Present address: Institute of Arctic and Alpine Research, University of Colorado, Boulder, CO 80309, USA.
†To whom correspondence should be addressed. E-mail: vasilii.petrenko@colorado.edu